

Additive Manufacturing of Nickel Superalloys: Opportunities for Innovation and Challenges Related to Qualification



S.S. BABU, N. RAGHAVAN, J. RAPLEE, S.J. FOSTER, C. FREDERICK, M. HAINES, R. DINWIDDIE, M.K. KIRKA, A. PLOTKOWSKI, Y. LEE, and R.R. DEHOFF

Innovative designs for turbines can be achieved by advances in nickel-based superalloys and manufacturing methods, including the adoption of additive manufacturing. In this regard, selective electron beam melting (SEBM) and selective laser melting (SLM) of nickel-based superalloys do provide distinct advantages. Furthermore, the direct energy deposition (DED) processes can be used for repair and reclamation of nickel alloy components. The current paper explores opportunities for innovation and qualification challenges with respect to deployment of AM as a disruptive manufacturing technology. In the first part of the paper, fundamental correlations of processing parameters to defect tendency and microstructure evolution will be explored using DED process. In the second part of the paper, opportunities for innovation in terms of site-specific control of microstructure during processing will be discussed. In the third part of the paper, challenges in qualification of AM parts for service will be discussed and potential methods to alleviate these issues through in situ process monitoring, and big data analytics are proposed.

<https://doi.org/10.1007/s11661-018-4702-4>

© The Minerals, Metals & Materials Society and ASM International 2018

I. INTRODUCTION

ADDITIVE manufacturing (AM) is considered to be a disruptive technology^[1] by enabling engineers to make complex-shaped component with a simple process flow that transitions from computer-aided design file to final part, rapidly.^[2–4] Based on this capability, innovative designs for turbine can be achieved by adopting AM for nickel-based superalloys.^[5] AM may also provide advantage by influencing heat transfer and pressure loss within the turbine components by incorporating wavy microchannels.^[6] Furthermore, AM also leads to unique surface properties due to spatial variations in melt pool shapes, *e.g.*, in contour melting, and will influence gas flow through the channels.^[7] It is well known that advanced geometries, *e.g.*, shaped film cooling, will lead to improved performance.^[8] In this regard, electron beam–powder bed fusion (E-PBF)^[9–11] and laser

beam–powder bed fusion (L-PBF)^[12,13] have shown the potential for processing of nickel-based superalloys.^[14,15] The direct energy deposition (DED) processes can be used for repair and reclamation of nickel alloy components.^[16] However, we need to consider the whole gas turbine as an engineering system and advances in every component design has to be evaluated and qualified within the context of the overall performance. The above question is being addressed from different aspects by various research groups across the world and are summarized in Table I. It is indeed clear the innovations related to process modifications, controls, powder processing and modifications, metallurgy, modeling, and property measurements are being pursued at a rapid pace. The current paper provides an overview of opportunities for innovations and qualification challenges with respect to deployment of AM for nickel-based superalloys, based on published literatures and ongoing research.

II. OVERVIEW OF PHYSICAL PROCESSES

In order to qualify high value-added nickel-based superalloy components made by AM, we need to understand various physical phenomena that occur during processing.^[17] Critical review of the literature^[18] clearly demonstrates that the metal additive

S.S. BABU, C. FREDERICK, and M. HAINES are with Mechanical, Aerospace and Biomedical Engineering, The University of Tennessee, Knoxville, 407 Dougherty Engineering Building, 1512 Middle Drive, Knoxville, TN 37934. Contact e-mail: sbabu@utk.edu
N. RAGHAVAN, R. DINWIDDIE, M.K. KIRKA, A. PLOTKOWSKI, Y. LEE, and R.R. DEHOFF are with the Oak Ridge National Laboratory, Oak Ridge, TN. J. RAPLEE is with Arconic, Pittsburg, PA. S.J. Foster is with Oerlikon, Charlotte, NC.

Manuscript submitted March 25, 2018.

Article published online June 1, 2018

Table I. Summary of Published Research Related to Additive Manufacturing of Nickel Alloys

Topic	Research Directions and Findings	References
Selection of Appropriate Processes	literature related to selection of different metal additive manufacturing for nickel-based superalloys	Refs. 70, 71
Powder Characteristics and Pre-processing	correlation of powder characteristics and pre-processing of powders to change flow and thermal properties and avoid issues during additive manufacturing	Refs. 72, 73
Process Parameter and Beam Scanning Optimization and microstructure control	process parameter and beam scanning paths optimizations to reduce the porosity and also the cracking tendencies by manipulating thermal and mechanical boundary conditions	Refs. 74–80
Alloy Design Approach	development of new alloys specifically suited for additive manufacturing	Refs. 81, 82
Process, Defects, Microstructure and Properties Correlations	correlation of the solidification microstructure, solid-state transformation, dislocations and precipitation sequences to cracking and properties	Refs. 83–89
Post Processing and AM Property Characterization and Properties	geometrical, microstructural and property changes during post-process heat treatment and hot-isostatic pressing, as well as, property evaluations (oxidation, cyclic testing and creep)	Refs. 90–98
Residual Stress and Distortion	role of processing parameters on the residual stress and distortion, as well as, measurement technology and results	Refs. 29, 99, 100
Deployment in Applications	outstanding Issues related to cracking and deployment in the service	Refs. 6, 7, 101
In Situ Monitoring and Qualifications	using thermal, optical and chemical sensing during AM	Refs. 55, 102–107
Integrated Computational Materials Engineering	using analytical and high-performance computing model for geometry, microstructure and property rationalization and optimization	Refs. 49, 50, 108–113

manufacturing is nothing but multi-pass micro-welding with complex boundary conditions imposed by the geometry and beam scanning strategies. This similarity of the physical processes between welding and AM is articulated with typical observations (see Figure 1) from L-PBF processing of Inconel 718 nickel-based superalloy.^[19]

Laser powder bed fusion AM of nickel superalloys is conducted in a protective chamber with dynamic argon flow to avoid oxidation or gas dissolution. To melt specific locations, a laser beam is scanned on top of the powder bed with different focal sizes and power. The absorption of laser beam leads to melting of the powder in the *i*th layer and also some remelting of the (*i*-1)th solid layer. The dynamics of melting and the melt-pool shapes are dictated by the scan strategy in the *x-y* plane. As the building progresses in the *z*-direction with pre-determined geometrical cross sections, one may observe the evolution of porosity, cracks, solidification grain structure, solid-state transformations, and plastic deformations (see Figure 1). In turn, all the above physical phenomena lead to spatial variations of microstructure and properties. In Figure 1(a), spatial variations of porosity, as well as, rough surfaces close to the edge of the build are observed. These porosities often emanate due to incomplete remelting of (*i*-1)th layer. The observed melt pool shapes and their variations in *x-y* surface and *x-z* cross section (Figures 1(b) and (c)) are indeed similar to multi-pass welding,^[20] with only caveat that the shapes of melt-pools and orientations are not maintained at each and every layer. Such variations are expected due to changes in energy

absorption of powders^[21] and the stability of molten liquids due to large transients in heat and mass transfer.^[22] One of the striking features of the *x-y* surface morphology is the presence of waviness due to overlapping melt-pool tracks (Figure 1(d)). These measurements show that the periodicity of the waviness can be in different length scales, ranging from sub- μm scales dictated by the surface ripples to largest scales sub-mm pertaining to the hatch distances. Based on welding metallurgy knowledge, we also postulate that these liquid-solid interface instabilities will manifest itself in the solidification microstructure.^[23] This is indeed confirmed by AM researchers across the world and electron backscattered diffraction (EBSD) image from Inconel 718 (Figure 1(e)) is shown as confirmatory evidence.^[19] The solidification grain structure can also be manipulated by addition of inoculants during welding.^[24] The translation of the same phenomenon to AM was recently confirmed by addition of nano-functionalized aluminum powder to the melt pool.^[25] It is known from literature that the welding processes with severe thermal gradient lead to excessive amount of thermal stress, which in turn leads to permanent plastic deformations. The accumulated plastic strain and subsequent thermal cycling may lead to the formation of dislocation cell structure (see Figure 1(f)). Similarity of the dislocation cell structure during welding^[26] and AM^[27] is also confirmed by observation of dislocation cell structure stainless steel builds made by AM. Similar to welding, the presence of permanent plastic deformation and its gradients may also lead to residual stress, which may be inferred from the hardness variations (see Figure 1(g))

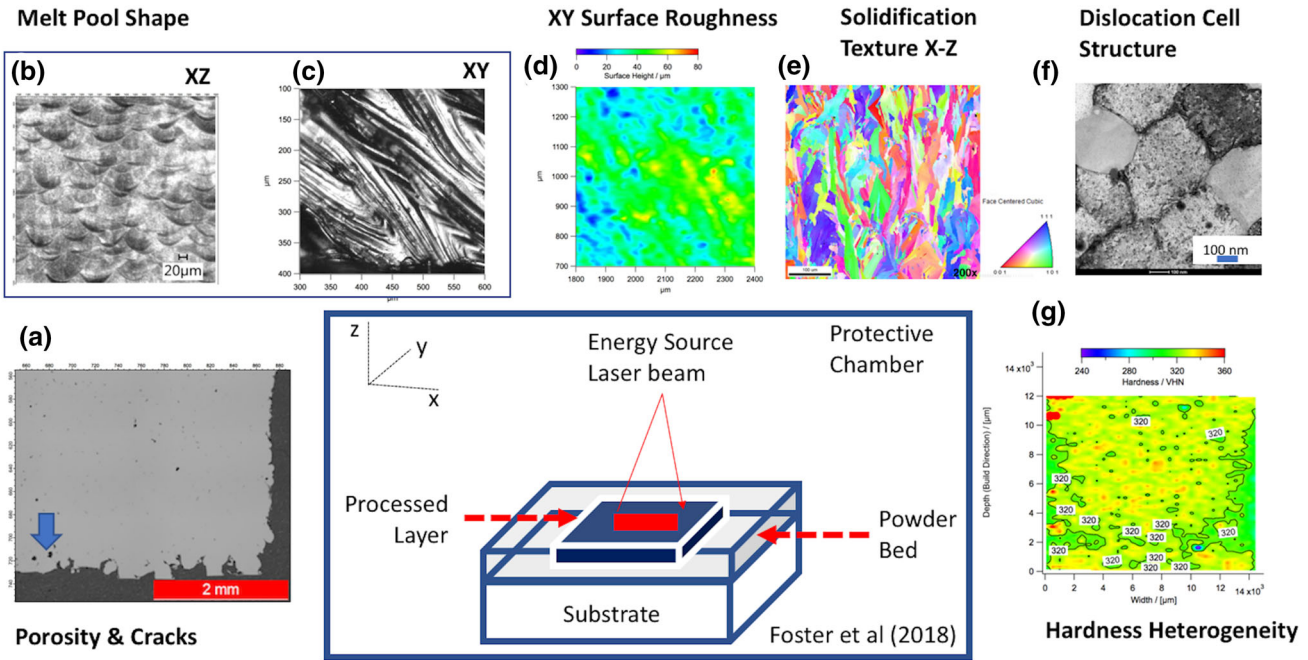


Fig. 1—Schematic illustrations of challenges faced by additive manufacturing of nickel-based superalloys (Inconel 718) brought about by the complex interactions between heat and mass transfer, solidification, solid-state transformation, and plastic deformations. (a) Preferential formation of lack of fusion porosity and rough surfaces near the edges of the build can be seen. Optical observations of large changes in 3-dimensional shape of melt-pools across the build in (b) x - z and (c) x - y sections. (d) Measured surface heights in the x - y surface illustrate the roughness in different length scales. (e) EBSD images showing large variations in crystallographic texture. (f) Low-angle grain boundary associated with high dislocation density with FCC matrix can be observed in the as-deposited condition; (g) All of the above variations lead to large heterogeneity of hardness within the build.

across the whole build.^[28] Recent publications have confirmed that these plastic strain gradients lead to large residual stress build up across the builds.^[29] The above discussions demonstrate that the vast knowledge in the welding literature related to process-structure-property (PSP) linkages can be leveraged for the AM of nickel-based superalloys. In the following sections, pathways to accelerate the adoption of AM of nickel-based superalloys is presented with examples from published literature.

III. COMMONALITY OF WELDABILITY AND ADDITIVE MANUFACTURABILITY

In this section, let us evaluate the similarity between weldability and additive manufacturability using an example scenario. Often nickel-based superalloys are classified based on their ability to be welded. In 2001, Dye, Hunziker and Reed^[30] published a paper, in which they used phenomenological models to develop weldability maps for thin sheets of Alloy 718 (2-mm thick) based on equations describing different defect formations. This graph is reproduced in Figure 2 with typical beam velocities used for power bed melting process.

It is indeed clear that during thin sheet welding of nickel alloys, it is impossible to produce sound welds above 5 mm/s. In contrast, published literature from nickel alloys show that it is indeed possible to produce sound L-PBF builds even with laser scan velocities

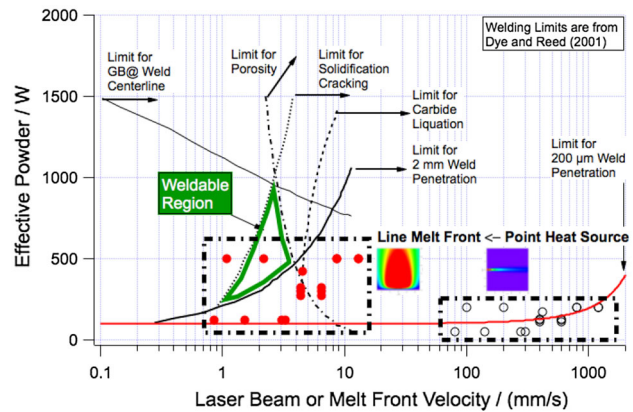


Fig. 2—Comparison of weldability map (data were extracted from reference 30) for alloy 718 with experimental conditions relevant to L-PBF processing. By correcting for changes in the melt pool shape, the L-PBF process parameters can be interpreted (red-filled circles) as line heat source with melt-front velocities similar to that of conventional welding.

greater than 100 mm/s.^[31] These data may appear to be discrepancy at first glance but can be rationalized based on the heat transfer conditions that prevail during L-PBF. During AM processes, the laser beam scans the cross section to be melted by moving back and forth with a predetermined scan length. At the end of reaching a scan length, the laser returns to the original location and offsets itself by hatch distance. Thermal diffusion

distance perpendicular to the laser scan direction can be calculated by using simple equation given here^[32]: $\delta \approx \sqrt{2\alpha\Delta t}$. In this equation, α is thermal diffusivity and Δt is the time interval for a given laser scan to return to the same location in a powder bed. If this distance is comparable to the hatch distance or laser beam focal diameter, one can conclude that the laser power distribution is no longer similar to ellipse, rather a line heat source moving at slower velocities comparable to that of the welding of thin sheets.^[33] The systematic increase in laser scan velocity in AM for a given hatch distance, the power distribution will go through transitions from *point* to *line* to *area* to *volume* heat source as a function of geometry being processed.^[34] Interestingly, these transitions based on the modifications of scan paths are routinely used during cladding, surfacing or welding operations^[35–38] relevant to nickel-based superalloys.

The above discussions indicate that additive manufacturing should be evaluated based on the size, shape, and velocity of molten pool as a function temporal and spatial coordinates with reference to the geometry being manufactured and not the velocity of energy source alone.

IV. CHALLENGES: MICROSTRUCTURAL AND MECHANICAL HETEROGENEITY

Among all the metal additive manufacturing processes, the most used process is the direct energy deposition (DED), originally developed by researchers from Sandia National Laboratory^[39,40] and referred as laser engineered near-net shaping (LENS). This process,

based on directed laser energy and powder delivery, is the most viable process for repair of small- and large-scale nickel-based superalloy components through layer-by-layer deposition. During routine DED processing for repair of alloy 718 components, two kinds of heterogeneities are observed,^[16] *i.e.*, (1) crystallographic texture and (2) hardness variations, as a function of build height (see Figure 3).

A. Crystallographic Heterogeneity

EBSD imaging from two distinct locations within a build is summarized in Figure 3. In Figure 3(a), three distinct regions of crystal orientations can be observed, as outlined by rectangular boxes A, B, and C. In the region A, the extent of misoriented grains is at 36 to 39 deg to the build direction. In region B, although the misorientations are at 85 to 88 deg, the aspect ratio of these grains is very high. This region coincides with the location of contour beads. Interestingly, in region C, the fraction of misoriented grains increases, while still maintaining the growth direction at about 48 to 53 deg. This region corresponds to hatch-melt part of the builds. Similar analyses were performed in a region that is far from the substrate region (see Figure 3(b)). Interestingly, the area fraction of the misoriented crystal growth (*i.e.*, in region C) has increased in comparison to regions A and B. Detailed analyses show that the crystal orientation range increased from 56 to 60 deg. This trend of increase in the misorientation angle is also seen in the regions A and B. This change in crystal growth behavior at different heights of the build is attributed to change in the weld pool shape and also reduction in the thermal gradients. The above conclusion was arrived by

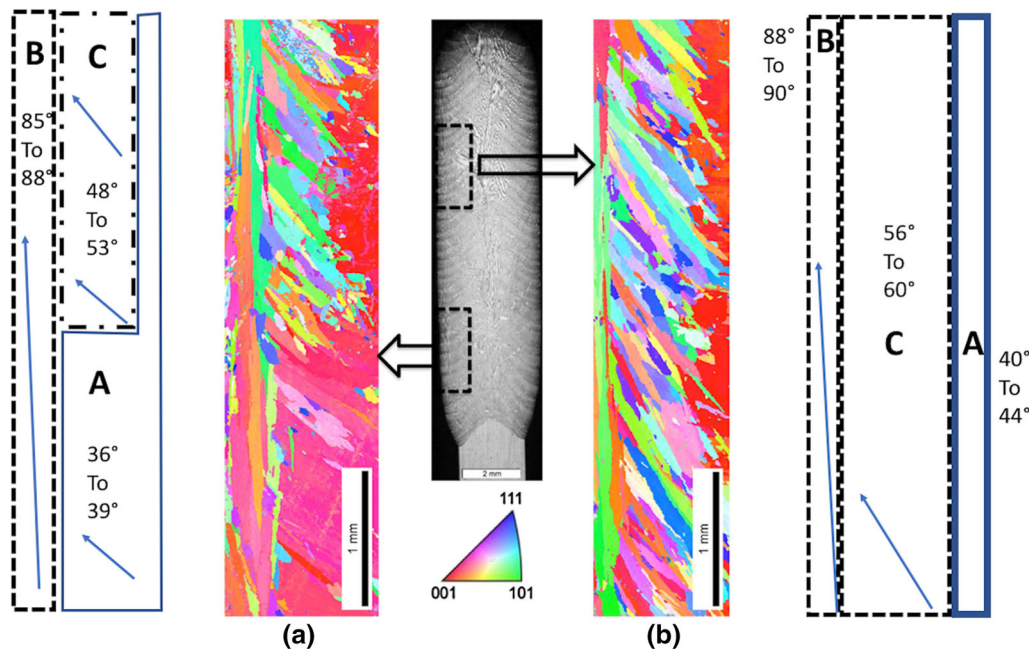


Fig. 3—Overview of crystallographic heterogeneity in two different build regions on Inconel 718 processed by DED; (a) closer to the substrate and (b) closer to the top region. The schematic diagrams on the left and right side show the angle of misorientation of major axes of FCC solidification grains with reference to build direction. Reprinted from Ref. [16] with permission.

estimating the melt pool boundary orientation to the build direction in the hatch melt areas. The melt pool boundary based on the etching contrast, close to the substrate, was inclined at -42 to -45 deg with reference to build direction. If we assume that crystal growth occurs along the maximum thermal gradient direction that is perpendicular to this boundary, we would expect crystal growth to occur along $+48$ to $+45$ deg. Similar analyses were performed for the top region. The boundary orientation was found to be -38 to -40 deg. The expected crystal orientation is $+52$ to $+50$ deg. Although, our predicted growth direction does not match the observed growth, the trends of increasing misorientation were confirmed. These results point to the importance of melt pool shape as a function of location and time.

B. Microstructural Heterogeneity

The salient features of mechanical heterogeneity in the Inconel 718 build and the rationalization of the same are summarized in Figure 4. The hardness map (Figure 4(a)) shows a large variation spanning from 200 to 450 VHN. The hardest region (location 2) observed closest to the substrate region and the softest region (location 6) at the top of build. It is well known that the strengthening of alloy 718 occurs due to precipitation of both γ'' and γ' precipitates, which in

turn depends on the overall thermal signatures below the solvus temperature. Typical thermal signatures were calculated using a commercial finite element code^[41] for locations 2, 4 and 6 (see Figure 4(b)). The data show that, in all the targeted locations, thermal signatures oscillate above and below the solvus temperature of both γ'' and γ' precipitates. The number of thermal gyrations in the precipitation temperature range is more for the location 2 than that of location 6. These thermal signatures were coupled with simultaneous transformation kinetics (STK) model^[42] and the extents of both γ'' and γ' precipitation were calculated. Even with repeated growth and dissolution, the calculations showed that the extents of precipitation in location 2 are higher than that of locations 4 and 6. Detailed microstructure analyses confirmed that the region 6 has less amount of precipitates (see Figure 4(c)) even close to the interdendritic regions. The bright region in this image corresponds to laves phase that forms during the last stages of solidification. In contrast, the region 2 contains copious amount of precipitates in both inter- and intra-dendritic regions (see Figure 4(d)). High-resolution transmission electron microscopy conformed that these are predominantly γ'' precipitates. It is noteworthy, that the above mechanical heterogeneity may not be generic and will be a strong function of geometry of the part, which in turn changes thermal cycles.

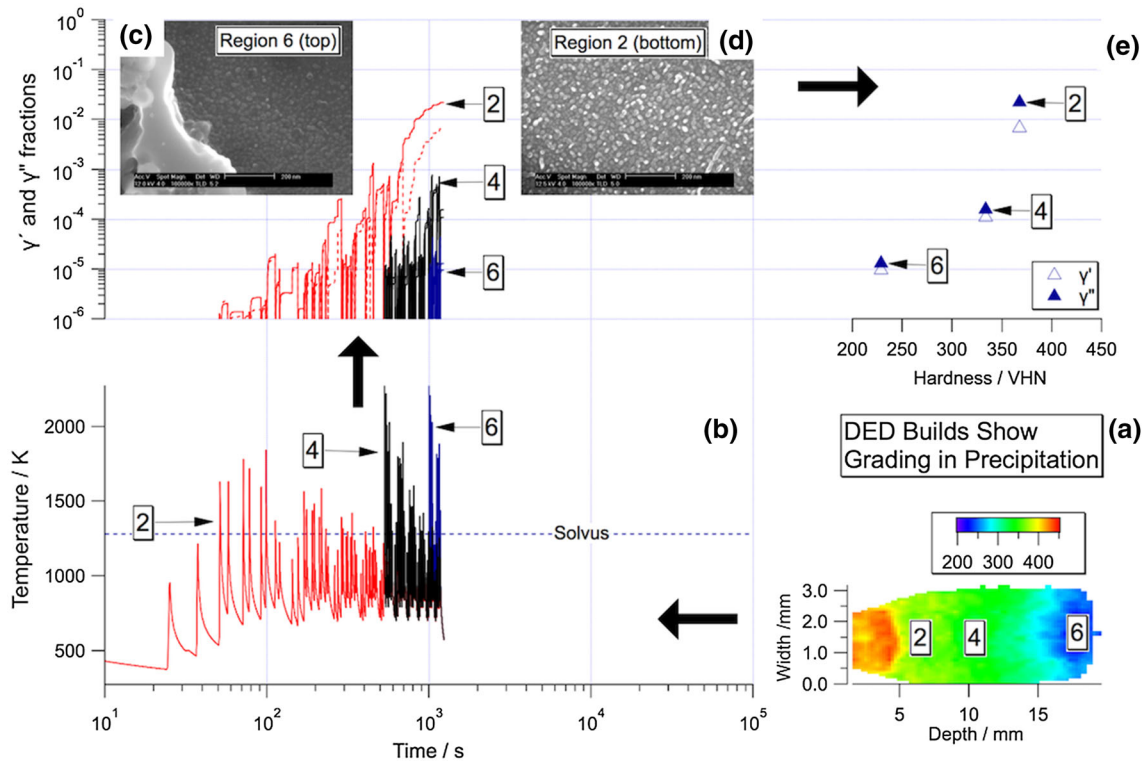


Fig. 4—Overview of mechanical heterogeneity in Inconel 718 build region processed by DED. (a) The hardness map shows mechanical heterogeneity as a function of depth starting from substrate to top of the build. (b) Predicted thermal cycles in locations 2, 4, and 6 show large differences in number of gyrations below and above the solvus temperature. Scanning electron microscopy images from the (c) top region showing only a small amount of precipitates close to the interdendritic regions, in contrast to (d) the bottom region showing a copious amount of precipitates. (e) Predicted volume fraction of precipitates at different locations show a log-linear relationship with measured hardness.

The above discussions confirmed that components produced by AM are processes that are prone to crystallographic and microstructural heterogeneities. This leads to the following question: is there a possibility of using this limitation to our advantage to induce site-specific microstructure?

V. OPPORTUNITIES: SITE-SPECIFIC CONTROL OF MICROSTRUCTURE

A. Role of Alloy Chemistry

Due to the inherent nature of scanning strategies associated with energy delivery in both E-PBF and L-PBF processes, it is quite conceivable to induce spatial and temporal variations of melt pool shape, G , R , as well as, thermal gyrations. In early 2014, Dehoff *et al.*,^[43] used raster and spot melting in specific locations to arrive at site-specific columnar and misoriented solidification grains. The selection of either columnar or equiaxed grain structure is related to the liquid-solid (l/s) interface instability.^[44,45] It is indeed possible to predict columnar to equiaxed solidification transition (CET), as a function of thermal gradient ($G_{l/s}$) and l/s interface velocities ($V_{l/s}$) based on dendrite tip temperature (T_d), with interface response function theories. The calculations are performed by solving the coupled equations^[46] that describe the (k_v^i) kinetic solute partitioning coefficient, (m_v^i) non-equilibrium slope of the liquidus, dendrite tip radius (R), and ($c_{l/s}^i$), concentration at l/s interface, as a function of $V_{l/s}$ and $G_{l/s}$.

$$k_v^i = (k_o^i + a_o [V_{l/s}/D_i]) / (1 + a_o [V_{l/s}/D_i]), \quad [1]$$

$$m_v^i = m_o^i (1 - k_v^i [1 - \ln\{k_v^i/k_o^i\}]) / (1 - k_v^i), \quad [2]$$

$$4\pi^2 \Gamma (1/R^2) + \left(2 \sum_i m_v^i Pe^i (1 - k_v^i) c_{l/s}^{i*} \zeta_c^i \right) (1/R) + G_{l/s} = 0, \quad [3]$$

where

$$\zeta_c^i = 1 - 2k_v^i / \left(2k_v^i - 1 + (1 + (2\pi/Pe^i))^{0.5} \right) \quad [4]$$

$$c_{l/s}^{i*} = c_o^i (1 - [1 - k_v^i] Iv\{Pe^i\}) \quad [5]$$

$$T_d = T_L +$$

$$\sum_i \left(c_{l/s}^{i*} m_v^i - c_o^i m_o^i \right) - 2\Gamma/R - V_{l/s}/\mu - (G_{l/s} D_i / V_{l/s}) \quad [6]$$

With the calculated dendrite tip undercooling, we can calculate the effective undercooling (ΔT) and the fraction stray formation (ϕ) using Eq. [7] derived by Gaumann *et al.*^[36]

$$G = (1/(n+1)) \sqrt[3]{(-4\pi N_o / (3 \ln\{1 - \phi\})) (\Delta T)} \times (1 - \Delta T_n^{n+1} / \Delta T^{n+1}) \quad [7]$$

In Eqs. [1] through [7], k_o^i is the equilibrium partitioning coefficient between the liquid and solid; D_i is the interphase diffusivity; m_o^i is the equilibrium liquidus slope; a_o is the characteristic diffusion distance; Γ is the Gibbs-Thompson coefficient; Pe^i is the Peclet number given by $V_{l/s}/(2D_i)$; μ is the interface kinetic coefficient, and $Iv\{\}$ is the Ivantsov function that depends on the Peclet number. Furthermore, N_o is the pre-existing

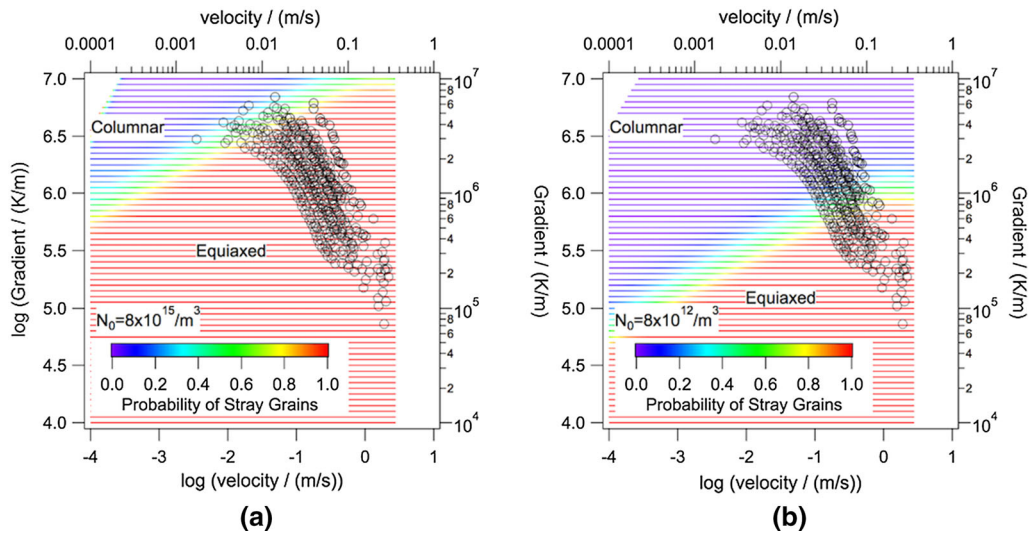


Fig. 5—The boundary between columnar to equiaxed solidification conditions are shown for (a) high-number ($8 \times 10^{15} \text{ m}^{-3}$) and (b) ($8 \times 10^{12} \text{ m}^{-3}$) low-number of pre-existing nuclei. The data points in the plot correspond to calculated values of G and R for typical E-PBF process.

nucleation number density ahead of the liquid-solid interface and ΔT_n is the undercooling for nucleation. Using thermodynamic information for a multicomponent system,^[47] Eqs. [1] through [7] can be iteratively solved to predict the dendrite tip temperature and thereby constitutional supercooling, as well as CET in a wide range of alloy systems. This model has been successfully applied to a wide range of multicomponent alloys.^[48] The above equations were solved for alloy 718 and the calculated solidification maps are shown in Figure 5. Since we do not know the N_0 values a-priori, two sets of calculations were performed to consider different pre-existing nuclei density. In addition, the calculated ranges of G and R for typical electron beam powder bed fusion (E-PBF) are also overlaid on the same plot. Raghavan *et al.*^[49,50] have shown methodologies to extract the G and R across the whole weld pool surface to arrive at volume fraction of the equiaxed grains throughout the melt-pool. The plots clearly demonstrate that for the high number of pre-existing nuclei (Figure 5(a)), the E-PBF processing conditions will lead to equiaxed grain structure, while the reduction of these nuclei will lead to mixture of columnar and equiaxed grain growth.

Currently, it is difficult to estimate the N_0 values *a priori*. However, one can modify this by adding inoculants to the melt pool. As mentioned earlier, the role of pre-inoculants on the equiaxed grain formation is well known in the welding metallurgy starting with classic work by Villafuerte *et al.*^[24] The extension of this concept to laser powder bed fusion process of aluminum was confirmed by Martin *et al.*^[25] A careful analysis of Figure 5 also shows that variations in G and R brought about by the transient processing conditions have stronger effect in comparison to the alloy modifications.^[51] This leads to a fundamental question, will these G and R values generic to the E-PBF process be

sensitive to beam scanning strategy and/or geometry of the part?

B. Role of Geometry

Lee *et al.*^[52] have explored the role of geometry for a given raster beam scanning during E-PBF process. In this work, they calculated the transient G and R values during the final stages of solidification using finite element methods. The plot shows that a simple change in cube geometry from 16 mm × 16 mm to 20 mm × 20 mm cross section may lead to many order of magnitude change in terminal liquid-solid interface velocity, *i.e.*, 2×10^{-3} to 1×10^{-1} m/s with smaller change in thermal gradients. This leads to fundamental question; will thermal signatures be different or the same for complex geometries?

In order to answer this question, high-speed video of electron beam scanning was recorded while melting a complex geometry shown in Figure 6. The original movie can be accessed from the following internet link.^[53] The image at two different time frames (Figures 6(a) and (b)) clearly demonstrates spatial variations of brightness during the build process. If we assume that these intensities are proportional to the temperature, the data confirm spatial and temporal variations of temperature gradients. The next task is to understand whether these variations have random modality or not. The optical intensity at different locations is extracted and plotted in Figure 6(c). The plots show that the signatures can be grouped into two broad categories depending on the probed location. The top-row of the images (group 1) show many re-melting and solidification events with saturated image intensity. In contrast, the group 2 show only one or two re-melting and solidification events. The differences between these groups are related to fundamental parameters of beam

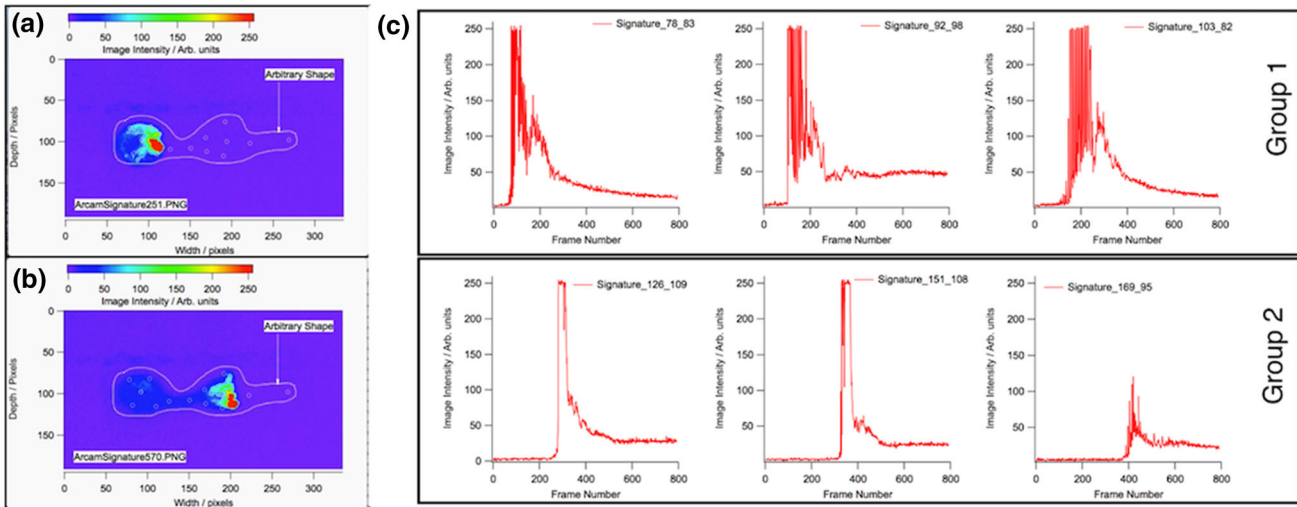


Fig. 6—Overview of electron beam scanning transients during E-PBF processing of a complex geometry at two different time intervals (*a*, *b*) showing the complex temperature distributions. (*c*) The optical intensities at different locations are extracted to analyze commonality of thermal signatures at these locations.

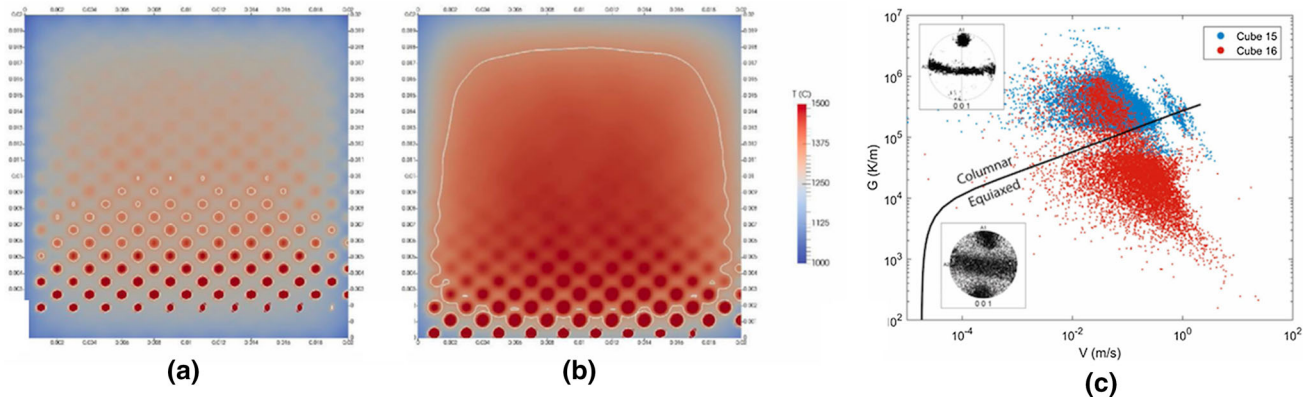


Fig. 7—A snap shot of the simulated surface melt pools for the (a) cube 15 and (b) cube 16 processing conditions. (c) Values of predicted G and R overlaid on top of the CET curve for alloy 718 predicted with calibrated N_0 value of 10^{11} m^{-3} . Reprinted from Ref. [34] with permission.

scanning attributes: (1) approach pattern to the location; (2) time spent at that location and (3) departure pattern away from the location and repeat of these steps, if any. This analysis provided a pathway to control thermal distributions in complex geometry, *i.e.*, development of spot melting pattern enforcing similar thermal signatures at a given location.

C. Role of Beam Scanning Strategy

The data provided in Figures 5 and 6 stipulate two requirements to arrive at microstructure control: (a) Thermal signatures should lead to many orders of magnitude variations in G and R, as well as, (b) the signatures have to be reproducible for site-specific microstructure in a complex geometry. In this regard, published literature corresponding to spot welding^[54] provides a pathway. During spot welding on a large substrate, four distinct stages are observed. In the 1st stage, under the energy input conditions, the melt pool forms on a substrate and grows slowly dictated by the balance between the heat flux from the source and the heat transfer away from the melt pool. In the 2nd stage, the growth of melt pool arrives at equilibrium, and no size change is observed with time. At this point, the temperature gradient (G) would have reached the maximum and the velocity of liquid-solid interface velocity (R) is zero. In the third state, when the energy source switches off, the *l/s* interface starts moving at slow velocity and starts accelerating. In the third stage, due to shrinking melt pool shape and infinite heat sink, thermal gradients (G) drop drastically and the *l/s* interface velocity increases exponentially. Based on this knowledge, it is clear that if we can control the spatial and temporal locations of the spot melting patterns prudently, it is possible to meet the requirements laid out for microstructure control.

Practical implementation of the spot melting and solidification conditions for CET in a cube geometry was explored by Plotkowski *et al.*^[34] with E-PBF of alloy 718. In this work, instead of switching between raster and spot melting pattern, the researchers used a

simple innovative approach of controlling only the spot-on time. The processing conditions were designed by using a simple heat transfer analytical model capable of predicting the spatial and temporal thermal signatures, as well as, transient melt pool shapes. The calculated melt pool shape, G and R for two cubes (identified as 15 and 16) are shown in Figure 7 for the following beam scanning conditions, while keeping the preheat temperature, (1273 K), accelerating voltage (60 kV), current (19 mA), and point-to-point distance of spots at $500 \mu\text{m}$.

Cube 15 was processed with shorter (0.1 ms) spot-on time, while the cube 16 was processed with longer (0.25 ms) spot-on time. The calculations predicted that the melt pool shape for cube 15 (Figure 7(a)) will not grow beyond $500 \mu\text{m}$, which is selected as point-to-point distance, while melt pool size in cube 16 can be in the same scale of the cube cross-sectional area (Figure 7(b)). Interestingly, the plots show that the majority of G and R values relevant to the cube 16 lie below the CET line suggesting equiaxed grain formation, while most of the G and R values for cube 15 lie above the transition line suggesting columnar grain formation. The measured texture plots obtained by EBSD imaging of cubes that were processed under these conditions are also presented as inset pictures within Figure 7(c). The (001) texture plot confirms the tendency for the equiaxed grain formation in cube 16 compared to cube 15. However, there is a weak texture corresponding to (001) columnar structure development is seen even in Cube 16. With the above successful demonstration, the obvious next step is to extend the methodology to complex geometries.

D. Extensions to Complex Geometry

In this section, ability to control site-specific microstructure in a complex bracket geometry by E-PBF process was explored with alloy 718.^[55] Although, it is possible to induce spot melting conditions throughout complex geometries, optimization of spot melting conditions for complex geometry proved to be difficult. This is because of the sheer number of

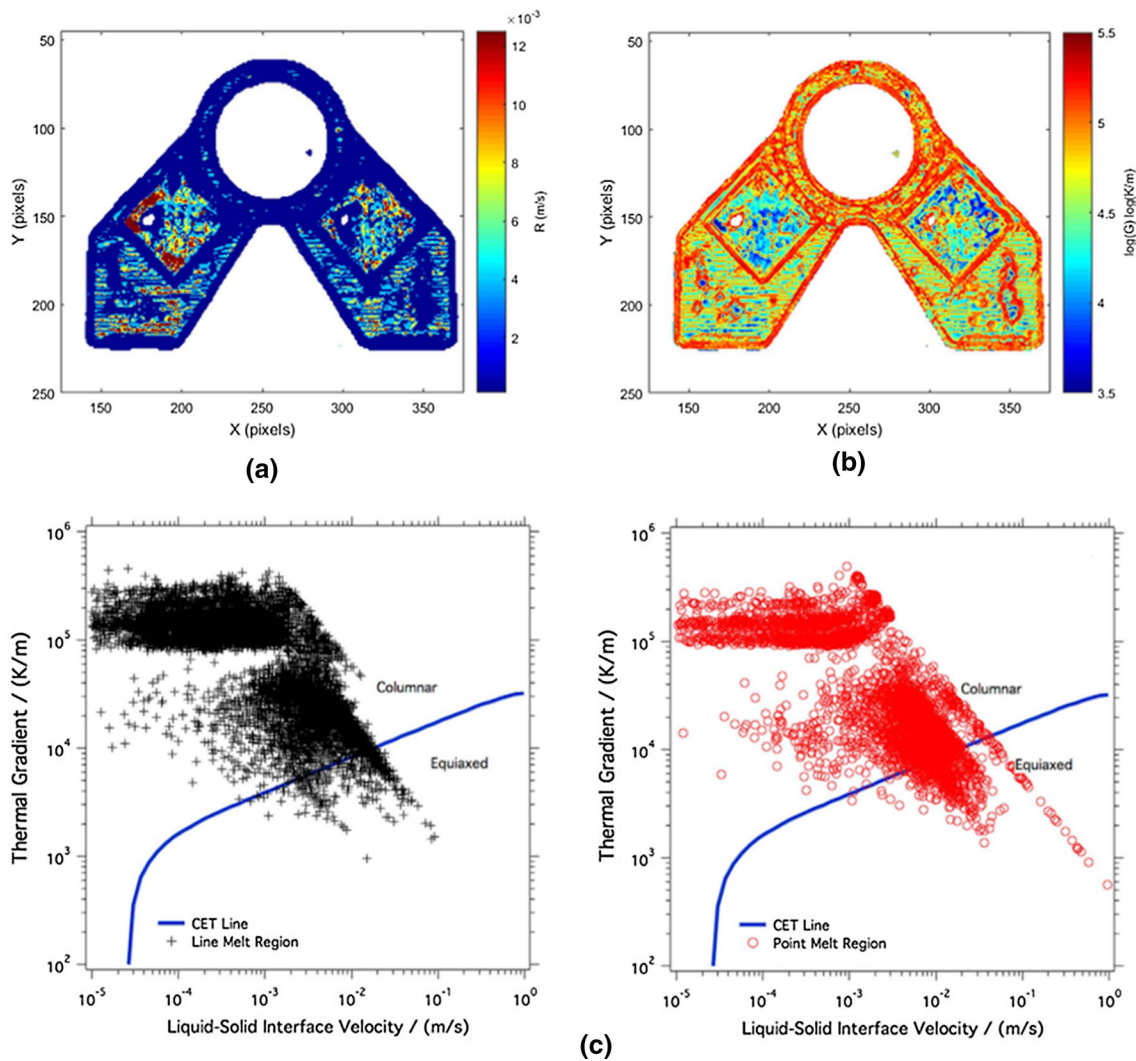


Fig. 8—Analyses of the *in situ* infrared imaging show the spatial variation of (a) G and (b) R across the bracket processed with raster and spot melting pattern. The image scale corresponds to G and R in logarithmic scale. (c) The measured G and R values are overlaid on top of the solidification map to induce transition from columnar to equiaxed transition. Reprinted from Ref. [55] with permission.

parameters needed for the heat transfer simulations. Therefore, a square region was selected for spot melting conditions and rest of the geometry was processed by standard raster conditions (Figure 8). To ensure that the Arcam® equipment reproduces the intended variations in G and R , an *in situ* IR imaging was also used while processing the complex geometry. In each and every layer, the build was made by alternating between raster and spot melting in specific locations. The spatial measurements of G and R for a given layer are shown in Figures 8(a) and (b). The measurements did show that there is a systematic decrease in thermal gradient in the spot melt pattern area outlined by a square. Interestingly, the variations in G and R are not straight forward across the whole layer; increased R values were observed both in raster regions and spot melted regions. The ring region always showed higher G and lower R values. The square region showed more often low G and higher R value. To understand the effect of these

measured G and R on solidification texture, the values are overlaid on the solidification maps (Figure 8(c)). Casual observation of the plots may not show a large difference between raster and spot melted regions. However, histogram analyses showed that large volume fraction of G and R values lies in the equiaxed part of the map for the spot melt regions.

To validate the above analyses, the solidification grain structure of these brackets was analyzed using EBSD imaging along the build direction (Figure 9). Although IR images showed certain amount of uncertainty, the square regions melted with spot patterns consistently lead to equiaxed solidification texture and a grain size in the order of $\sim 100 \mu\text{m}$. As expected, the ring region confirmed the presence of long, coarse ($\sim 300 \mu\text{m}$) columnar grains extending along the build direction. The above data essentially confirm the merit of simulation aided process parameter and beam scanning strategy as a function of location to arrive at site-specific

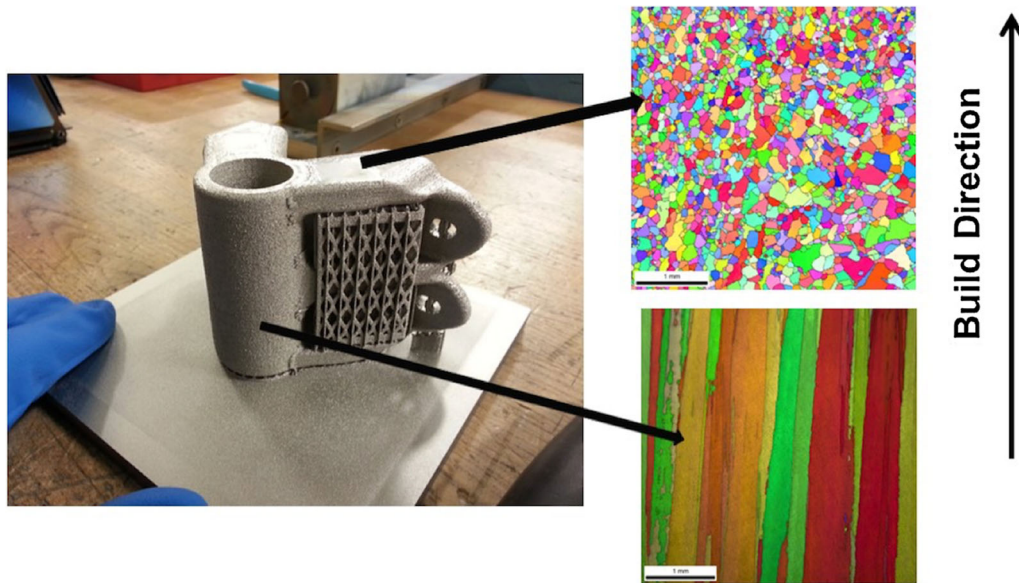


Fig. 9—Photograph of the completed E-PBF Alloy 718 bracket build with equiaxed grain formation in the spot melt region and also columnar grain formation in the raster melt region.

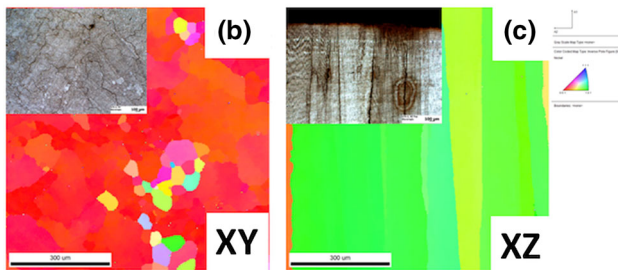
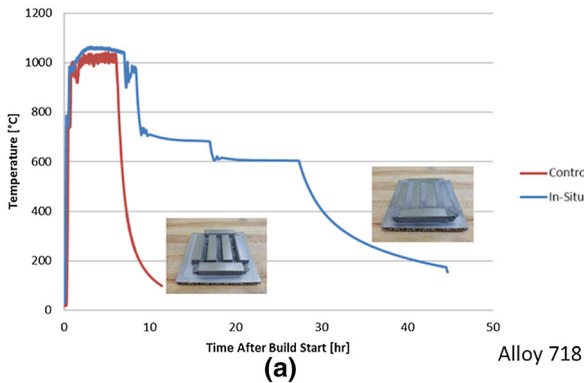


Fig. 10—Overview of the thermal signature during E-PBF processing of alloy 718 (a) with default parameters and surface melting strategy to induce an artificial *in situ* heat treatment. The insets show the condition of the final build after removal from the machine. EBSD images along the (b) XY and (c) XZ direction show that the columnar grain structure is preserved. The inset optical micrographs in (b) and (c) show the tendency for cracking along the FCC grain boundaries.

microstructure in a complex geometry made with nickel-based superalloy. This ability provides unique technical case for additive manufacturing of nickel-based superalloys.

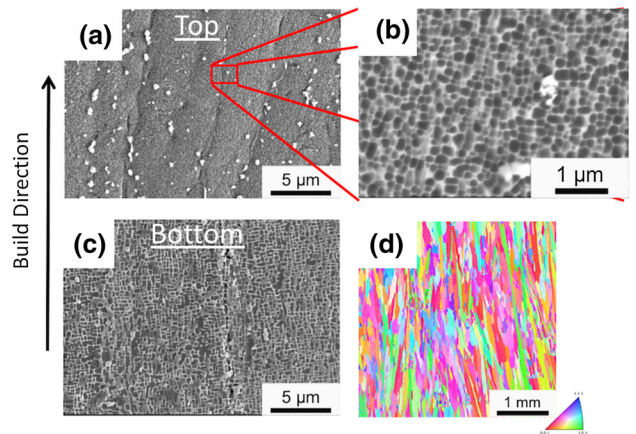


Fig. 11—Overview of microstructure of CM247 alloy sample processed by E-PBF process; (a) macrograph from the top region shows the columnar grains with interdendritic carbides and (b) fine cuboidal gamma prime precipitates. (c) The bottom regions exhibit similar grain structure with coarse cuboidal microstructures. (d) EBSD imaging shows predominantly columnar grain structure throughout the build heights.

E. Control of Solid-State Transformation

Although the earlier sections focused on solidification microstructure control, the need for controlling solid-state transformation was also understood. Babu *et al.*^[56] have shown that by controlling the cooling rate from a temperature above solvus temperature, the size, shape, and composition of the precipitates can be controlled in CM247 alloys. However, due to the E-PBF device limitations, on demand control of the cooling rate cannot be achieved. Instead, Sames *et al.*^[18] devised innovative surface melting strategies after completion of the build to introduce *in situ* heat treatment within the build chamber

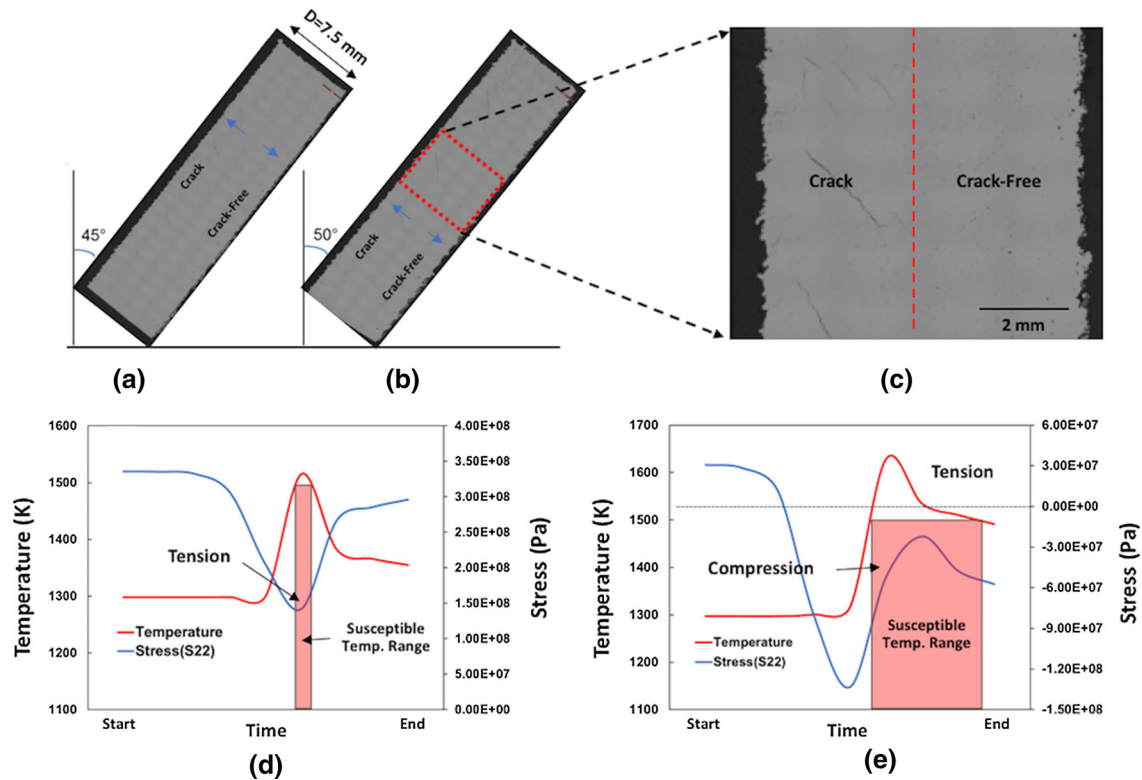


Fig. 12—Orientations of the build samples with different angles, *i.e.*, (a) 45 and (b) 50 deg to the build direction. (c) Optical microscopy analyses of the samples show consistent cracks in the left side of the sample. The predicted variation of temperature and stress across the (d) left and (e) right side of the build. The shaded area corresponds to regions that would remain above a critical temperature where the partially solidified regions are expected to be present.

itself. Comparison of thermal signatures, measured at the substrate plate, for typical E-PBF processing and in situ heat treatment shows the feasibility of solid-state transformation control (See Figure 10(a)). The above heat treatment cycles were designed based on calculated time-temperature-transformation (TTT) diagram for alloy 718 calculated using JMatPro® software. Although the above work showed the ability to maintain the same crystallographic texture (see Figures 10(b) and (c)) control the size of γ'' precipitate size distribution, this processing strategy leads to two challenges. First, due to high residence time at and above the solvus temperature, the powder particles sintered extensively. Second, due to inherent nature of precipitation and thermal stresses developed in the geometry, it led to cracking along the columnar grain boundaries.

F. Extension to High-Gamma Prime CM247 Superalloys

Since the normal welding or E-PBF processing of high gamma prime alloys relies on high preheat temperature just below or above the solvus temperature, the regions close to the substrate may experience prolonged aging at high temperature after the initial solidification. In contrast, the regions near the top of the region may only be exposed to shorter aging before the final cool down. This may lead to gradients in microstructure related to solid-state decomposition of FCC- γ matrix into mixture of γ , γ' phases. This phenomenon was

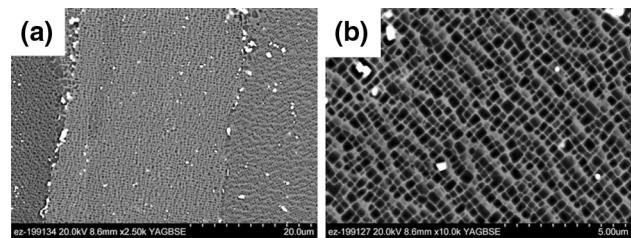


Fig. 13—Scanning electron microscopy images of post-processed CM247 alloy builds: (a) At low magnification, the columnar dendrite grains with interspersed with brightly imaging intermetallic and carbides along the grain boundaries and inside the grains can be observed. (b) High magnification showing uniform distribution of cuboidal gamma prime dispersed within the gamma phase.

confirmed by the characterization of a builds processed with CM247 alloy and E-PBF, as a function of depth (see Figure 11). Onset of precipitation and gradients across the Z-direction during processing may influence cracking tendencies of these alloys.

G. Asymmetric Cracking Tendencies in Mar-M-247 Alloys

In this experiment,^[57] cylindrical parts of 7.5 mm diameter were produced with Mar-M-247 alloy powders using standard raster pattern with E-PBF process. The samples were positioned at an angle to the build direction (45 to 50 deg). The preheat temperature was

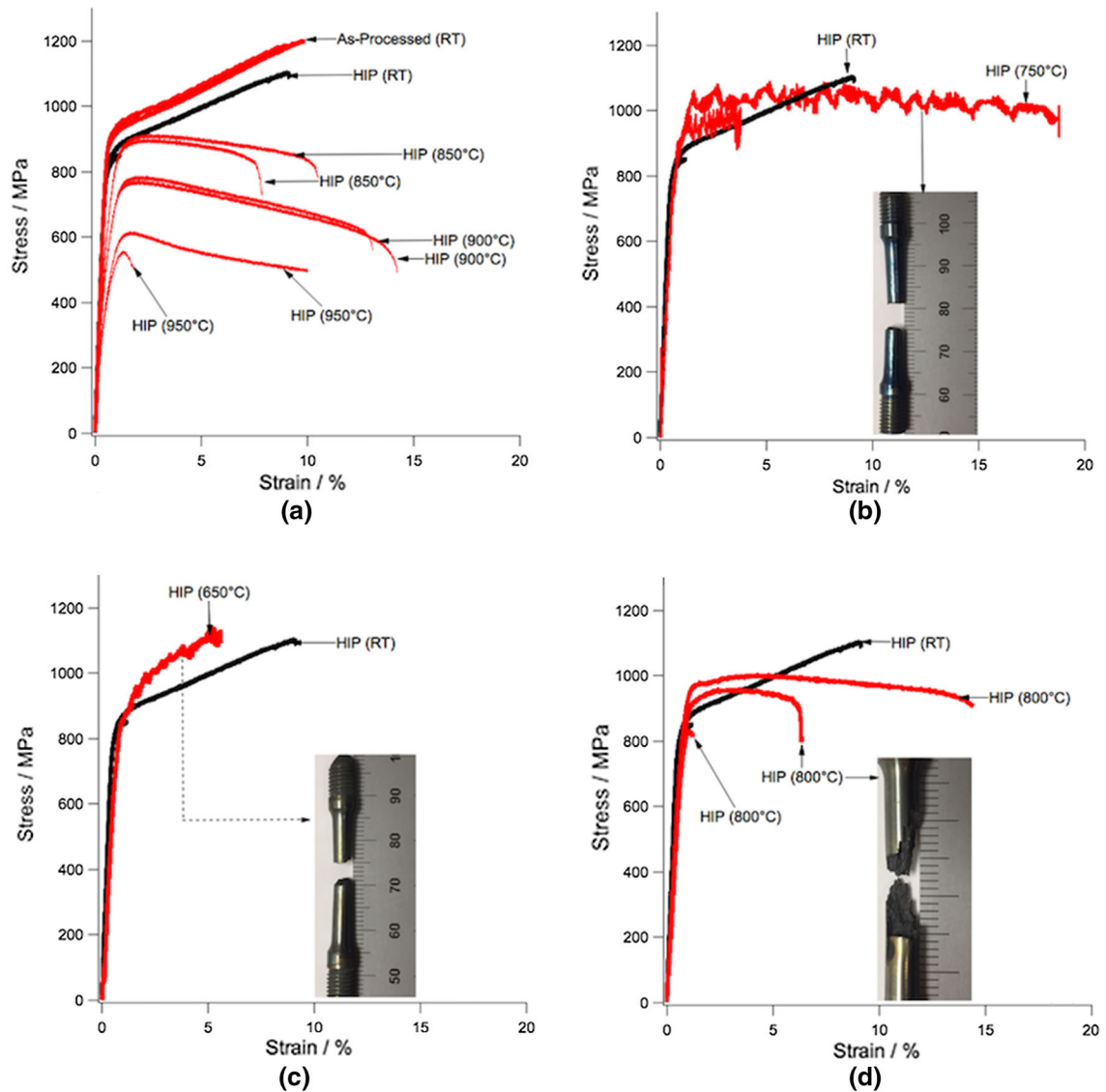


Fig. 14—Overview of all engineering stress-strain diagrams at different temperatures are compared with room temperature data obtained after hot isostatic pressing (HIP): (a) As-processed, HIP at 950 °C, 900 °C, and 850 °C, (b) HIP at 750 °C, (c) HIP at 650 °C and (d) HIP at 800 °C. The inset also shows the fracture mode of the samples tested at 650 °C, 750 °C, and 800 °C.

maintained at 1298 K. This temperature is indeed lower than the solvus temperature for the gamma prime which is calculated to be 1466 K. As a result, with the progress in the building process, there will be a wave of repeated nucleation, growth, and dissolution of gamma prime in locations just below the top melt regions. This is due to repeated heating to peak temperatures above the solvus temperature and cooling back to 1298 K. However, as the build progresses, the regions that are far below will be subjected to prolonged aging at 1298 K and will exhibit precipitate coarsening. Based on the welding cracking literature, the onset of precipitation in the heat-affected-zones will stifle the relaxation of thermal stresses. With the presence of tensile thermal stresses, there may be increased tendency for the weld cracking.

Careful analyses of the Mar-M-247 builds (see Figures 12(a) through (c)) showed tendencies for asymmetric cracking. The cracks were associated with

solidification grain boundaries with large misorientations and inter-dendritic microstructures and therefore classified as weld solidification cracking. Although thermal conditions relevant to solidification conditions are similar throughout the layer, the consistency of crack resistance on one side of the geometry requires further attention. Detailed thermo-mechanical analyses of E-PBF processing during ith layer were performed using finite element analyses for the raster scanning across disc shaped cross section at the intersection of the build plane and the cylindrical geometry. The results are summarized for the specific locations that show cracking and resistance to cracking (Figure 12). Interestingly, the simulations show that the tensile stresses develop on the left side of the sample and overlaps with the susceptible conditions for cracking. In contrast, although the right side of builds spend longer time in the susceptible region, the stresses in these regions are compressive, as a result, it will not lead to any cracking.

Such a close linkage between dynamic thermal stress evolution (tensile or compressive) and cracking tendency in nickel alloy welding was published by Feng *et al.*,^[58] Park *et al.*,^[38] and Yang *et al.*^[59] Therefore, future research should focus on managing thermal stress alignment across the build directions for a given geometry while performing the microstructure control.

H. Role of Post-Process Heat Treatments and Mechanical Properties

The above example suggests that there is a need for post-process hot-isostatic-pressure (HIP) treatments to heal the cracks and homogenize the microstructure. The validity of the above assumption was explored by subjecting the CM247 samples to the following HIP cycle: heating to 1503 K for 4 hours and quenched rapidly in Quintus® QIH9 furnace. Then, the samples were subjected to heat treatment at 1353 K for 2 hours and then secondary age at 1143 K for 24 hours. The microstructure after the above heat treatments is shown in Figure 13. The microstructure shows that the columnar nature of the matrix is maintained, while the precipitate microstructure was reset to uniform across the whole sample. This result confirmed that it is indeed possible to use post-process heat treatment to fine tune the solid-state microstructure, while maintaining solidification microstructure achieved by the process and beam scanning strategies.

In the next step, the role of this initial microstructure on high-temperature tensile strength was evaluated following standard ASTM standards for tensile testing. The stress-strain diagrams (Figure 14) show interesting features and are discussed below. The as-processed samples (Figure 14(a)) show higher yield strength and hardness compared to samples tested after HIP and heat treatment. The mechanical properties from HIPed samples tested at 850 °C to 950 °C were found to be consistently softer than room temperature properties. The total elongation appears to be inconsistent and is associated with changes in grain boundary carbides (see Figure 13). The stress-strain data measured at 650 °C, 750 °C, and 800 °C show that yield strength at these temperatures is higher than that of room temperature data. Furthermore, the samples tested at 650 °C and 750 °C show serrated flow. This phenomenon is similar to Portevin-Le Chatelier (PLC) effect observed in other nickel-based superalloys at low temperature (< 600 °C).^[60–62] The above mode of deformation was also associated with a flat fracture surface. In contrast, the samples deformed at lower and higher than this temperature range, failed to show any PLC effect. Currently, the mechanism for the PLC effects in our samples at high temperatures are unknown. Evaluation of the above samples under creep and creep-fatigue conditions are part of the ongoing research.

VI. FUTURE DIRECTION: QUALIFICATION OF AM COMPONENTS

The discussions in the previous sections provide early confidence that the nickel-based superalloys with targeted solidification microstructure and properties can be

achieved even in complex geometries with good high-temperature mechanical properties. However, there is one outstanding issue that is related to diagnosing the cracking tendency and defect formation which may be highly stochastic. The uncertainty is related to inherent variations in magnitude and directionality of thermo-mechanical strains and temperature gradients during E-PBF powder melting. This statement leads to the next fundamental question: is there any way to qualify these AM components without extensive post-process and destructive characterization?

Metallic components used in the gas turbines, operating at high stress, temperature, and harsh environment, go through extensive qualification based on available non-destructive-evaluation (NDE) and/or non-destructive-inspection tools. These NDE procedures should meet the strict requirements laid down by industrial standards. Even for traditional machining (*e.g.*, during hole making, turning and broaching), NDE tools (*e.g.*, eddy current inspection) do not always detect geometric and non-geometric anomalies.^[63] These NDE tools also have limitations due to the lack of automated interpretation. This leads to an important question: are there any specific challenges of using NDE tools for AM? In a classic review by Todorov *et al.*,^[64] various NDE techniques [Visual testing, Leak Testing, Liquid Penetrant testing, Process compensated resonant testing, electrical impedance spectroscopy, alternate current potential drop, eddy current testing, array eddy current testing, phase array ultrasonic testing, radiography testing, X-ray computed tomography, micro-focus X-ray computed tomography, Magnetic particle testing, microwave non-destructive testing, and terahertz imaging] were considered for the deployment to AM. Although the buried in defects can be accessed by volumetric evaluation tools such as computer-aided X-ray tomography, 100 pct detection of defects using this approach is not practical for gas turbine AM components. For example, neutron imaging tomography was used by Watkins *et al.*^[65] for NDI evaluation of residual stress and geometrical conformity of gas turbine blades. Nevertheless, these methodologies cannot be scaled to production environments.

Since the AM process relies on layer-by-layer melting, one can implement qualification of tools by comprehensive sensing and monitoring of thermal and surface displacements to arrive at three-dimensional representation of the geometry, as well as, spatial distribution of defects (*e.g.*, porosities and cracks) and microstructures. Preliminary evaluation of the hypothesis for solidification microstructure evaluation was presented already.^[55] In newer version of the E-PBF process equipment (*e.g.*, Arcam Q10+), it is possible to take near infrared image (NIR) images before and after each layer. The NIR image data may provide information of possible location of porosity, cracks, and also surface heights. These features often show up as bright regions in the NIR images. Recently, this methodology coupled with deep neural nets (DNN) was used to correlate the tensile failure of topology optimized part to regions with concentrated porosity.^[66]

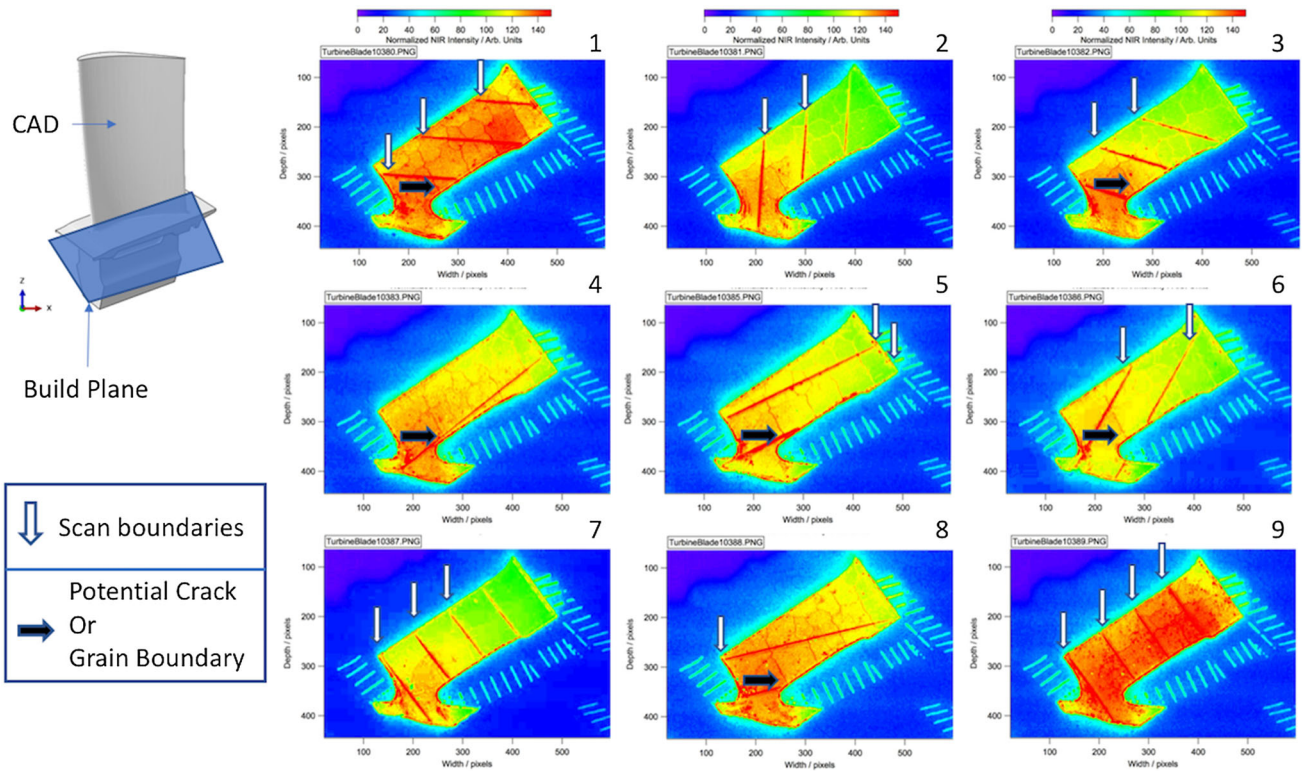


Fig. 15—Overview of sequential NIR images from consecutive nine layers near the platform region show the changing of the scan boundaries and consistent cracking pattern across many layers. Note the image scaling is affected by the surface features, orientation of the surface to the NIR camera and also the local remnant temperature.

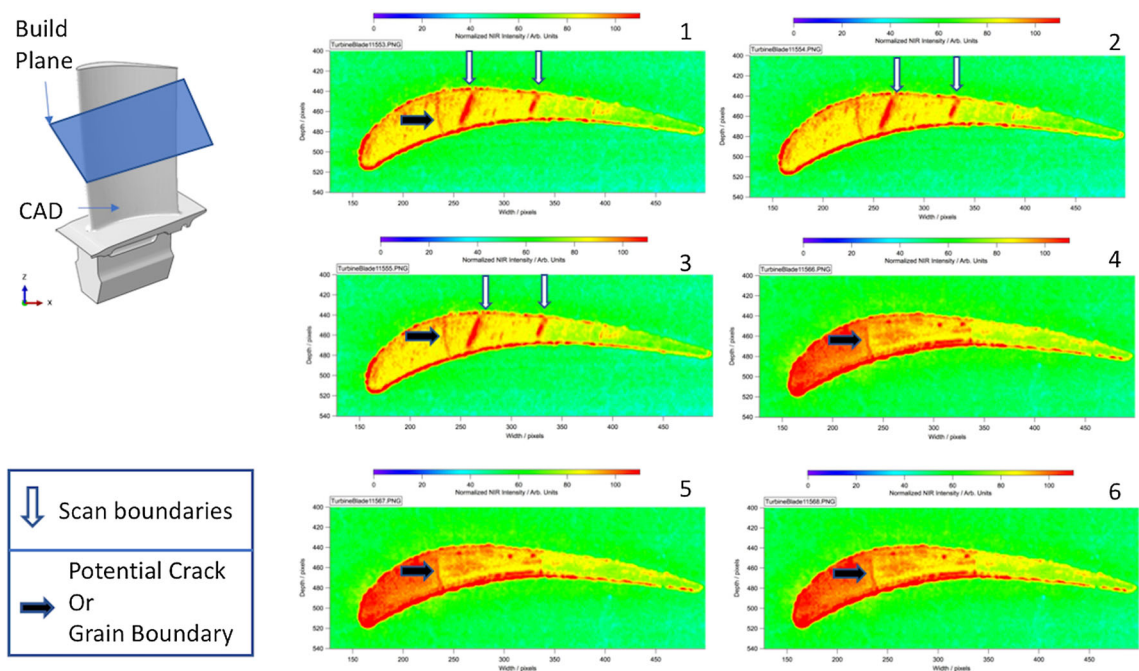


Fig. 16—Overview of sequential NIR images from consecutive six layers near the airfoil region shows remnant of one single crack across six layers. The IR intensity from the thick sections appears to blend with surrounding powder, except the boundaries which are expected to have small differences in heights due to contour melting.

Preliminary research on extending NIR methodology to diagnose the cracking tendency during processing Inconel 738 alloys, within a complex airfoil geometry, is

presented here.^[67] The blade geometry to be additively manufactured is shown in Figures 15 and 16. This complex geometry was tilted at a pre-determined angle

to the build direction to explore possible interactions of geometry and cracking tendency, similar to the experiment described earlier. The NIR images from the platform region during nine layers are presented in Figure 15. The images show both scan boundaries (white block arrow) and potential regions (dark block arrow) for cracking. Since the images are from XY section of the build plane, the cracks appear to outline the boundaries of columnar grains. Interestingly, some of the cracked locations appear to change directions when they interact with the scan boundaries and some of them continue on without any effect from scan boundaries. Although the image exposure time was maintained constant, one can clearly see that there is a large gradient of background illumination with each and every layer. Currently, this gradient is hypothesized to be the result of macro-scale surface distortions, similar to the one predicted by Prabhakar *et al.*^[68] The copious amount of cracking in the platform region (Figure 15) is attributed to higher mechanical restraints during melting.

This leads to the obvious question, will the tendency to crack reduce if we reduce the cross-sectional area in a given layer? The sequential NIR image data from airfoil region are summarized in Figure 16. As expected, the gradients in images were lower than that of the platform region. Only one crack was observed to be remnant in all six layers. Interestingly, these images are not able to capture all the scan boundaries, because these boundaries do not intersect with the sectional geometry of the airfoils for each and every layer.

Some of the deficiencies of this method also can be understood from the fact that intensity values bleed from the part to the surrounding powder also. This is related to the inherent variation of IR emissivity between powders and solid. The above NIR image analyses have to be automated similar to porosity detection using deep neural networks (DNN) and machine learning (ML) algorithms.^[69] With the completion of this crucial step, NIR images can be used as diagnostic tool for evaluating the complex nickel-based superalloy parts to be made by AM an industrial setting.

VII. SUMMARY

An overview of published and ongoing research demonstrates that the fusion-based metal additive manufacturing induces spatial and temporal variations of melt pool, thermal gradient, liquid-solid interface velocity, and thermal gyrations. These variations always lead to spatial microstructural and mechanical heterogeneities within a given geometry and processing conditions for wide range of nickel-based superalloys. However, with innovative beam scanning strategies, site-specific microstructure control can be achieved during AM. This hypothesis was conclusively proven using well-designed E-PBF melting experiments with alloy 718 powders, by coupling heat transfer models, solidification maps and in situ IR imaging. Approaches to control the solid-state transformation in the same alloy using in situ heat treatment were also explored and

lead to successful control of the precipitate morphology while maintaining the original (001) crystallographic texture. Nevertheless, similar to welding, extension of AM to high gamma prime alloys (*e.g.*, CM247, Mar-M-247 and IN 738 alloys) leads to cracking in geometries under severe thermal restraints. Post-process methods to heal the cracks and homogenize the microstructure using HIP and heat treatment in CM247 alloys show promising results. Qualification of the complex nickel-based superalloy geometry through near infrared imaging (NIR) is suggested as a way to understand the spatial variations of cracking as a function of beam scanning strategy and cross-sectional geometry.

ACKNOWLEDGMENTS

This research is based upon work supported by the US Department of Energy, Office of Energy, Efficiency, and Renewable Energy, Advanced Manufacturing Office under Contract Number DE-AC05-00OR22725. The United States Government retains and the publisher, by accepting the article for publication, acknowledges that the United States Government retains a non-exclusive, paid-up, irrevocable, world-wide license to publish or reproduce the published form of this manuscript, or allow others to do so, for United States Government purposes. The Department of Energy will provide public access to these results of federally sponsored research in accordance with the DOE Public Access Plan (<http://energy.gov/downloads/doe-public-access-plan>).

REFERENCES

1. B. Berman: *Business Horizons*, 2012, vol. 55, pp. 155–62.
2. W.E. Frazier: *JMEPEG*, 2014, vol. 24, pp. 1917–2928.
3. I. Gibson, D.W. Rosen, B. Stucker, Additive manufacturing technologies Rapid prototyping to direct digital manufacturing, Springer, Heidelberg, 2010. <https://doi.org/10.1007/978-1-4419-1120-9>.
4. D.D. Gu, W. Meiners, K. Wissenbach, and R. Poprawe: *Int. Mater. Rev.*, 2012, vol. 57, pp. 133–64.
5. B. Ealy, L. Calderon, W. Wang, R. Valentin, I. Mingareev, M. Richardson, and J. Kapat: *J. Eng. Gas Turbines Power*, 2017, vol. 139, p. 102102.
6. C.K. Stimpson, J.C. Snyder, K.A. Thole, and D. Mongillo: *J Turbomach*, 2017, vol. 139, p. 021003.
7. K.L. Kirsch and K.A. Thole: *Int. J. Heat Mass Transf.*, 2017, vol. 108, pp. 2502–13.
8. R.S. Bunker: *J. Heat Transf.*, 2005, vol. 127, pp. 441–53.
9. L.E. Murr, E. Martinez, X.M. Pan, S.M. Gaytan, J.A. Castro, C.A. Terrazas, F. Medina, R.B. Wicker, and D.H. Abbott: *Acta Mater*, 2013, vol. 61, pp. 4289–96.
10. H. Helmer, A. Bauereiß, R.F. Singer, and C. Körner: *Mater. Sci. Eng. A*, 2016, vol. 668, pp. 180–87.
11. M. Ramsperger, R.F. Singer, and C. Korner: *Metall. Mater. Trans. A*, 2016, vol. 47A, pp. 1469–80.
12. N.J. Harrison, I. Todd, and K. Mumtaz: *Acta Mater.*, 2015, vol. 94, pp. 59–68.
13. A. Basak, R. Acharya, and S. Das: *Metall. Mater. Trans. A*, 2016, vol. 47A, pp. 3845–59.

14. S. Das, D.L. Bourell, and S.S. Babu: *MRS Bull.*, 2016, vol. 14, pp. 729–41.
15. S.S. Babu, L. Love, R. Dehoff, W. Peter, T. Watkins, and S. Pannala: *MRS Bull.*, 2015, vol. 40, pp. 1154–61.
16. Y. Tian, D. McAllister, H. Colijn, M. Mills, D.F. Farson, M.C. Nordin, and S.S. Babu: *Metall. Mater. Trans. A*, 2014, vol. 45, pp. 4470–83.
17. T. Debroy, H.L. Wei, J.S. Zuback, T. Mukerjee, J.W. Elmer, J.O. Milewski, A.M. Beese, A. Wislonheid, A. De, and W. Zhang: *Prog. Mater. Sci.*, 2018, vol. 92, pp. 112–224.
18. W. Sames, F.A. List, S. Pannala, R.R. Dehoff, and S.S. Babu: *Int. Mater. Rev.*, 2016, vol. 61, pp. 315–60.
19. S.J. Foster, S.S. Babu, and A. Chaudhary: *Unpublished Research*, University of Tennessee, Knoxville, 2018.
20. R.C. Reed and H.K.D.H. Bhadeshia: *Acta Metall. Mater.*, 1994, vol. 42, pp. 3663–78.
21. S.S. Babu, R.A. Martukanitz, K.D. Parks, and S.A. David: *Metall. Mater. Trans.*, 2002, vol. 33A, pp. 1189–1200.
22. P.S. Wei: *J. Heat Transf.*, 2010, vol. 133, p. 031005.
23. A.C. Hall and C.V. Robino: *Sci. Technol. Weld. Join.*, 2004, vol. 9, pp. 103–08.
24. J.C. Villafuerte, H.W. Kerr, and S.A. David: *Mater. Sci. Eng. A*, 1995, vol. 194, pp. 187–91.
25. J.H. Martin, D.D. Yahata, J.M. Hundley, J.A. Meyer, T.A. Schaedler, and T.M. Pollock: *Nature*, 2017, vol. 549, pp. 365–69.
26. O.M. Barabash, S.S. Babu, J.M. Vitek, S.A. David, J.-W. Park, J.A. Horton, G.E. Ice, and R.I. Barabash: *J. Appl. Phys.*, 2004, vol. 96, pp. 3673–79.
27. Y.M. Wang, T. Voslin, J.T. Mckeown, J. Ye, N.P. Calta, Z. Li, Z. Zeng, Y. Zhang, W. Chen, T.T. Roehling, R.T. Ott, M.K. Santala, P.J. Depond, M.J. Matthews, A.V. Hamza, and T. Zhu: *Nat. Mater.*, 2018, vol. 17, pp. 63–70.
28. D. Qiao, W. Zhang, T.-Y. Pan, P. Crooker, S. David, and Z. Feng: *Sci. Technol. Weld. Join.*, 2013, vol. 18, pp. 624–30.
29. L. Kolbus, A. Payzant, P. Cornwell, T. Watkins, S.S. Babu, R. Dehoff, and C. Duty: *Metall. Mater. Trans. A*, 2015, vol. 46 (3), pp. 1419–32.
30. D. Dye, O. Hunziker, and R.C. Reed: *Acta Mater.*, 2001, vol. 49, pp. 683–97.
31. I. Yadroitsev, A. Gusarov, I. Yadroitsava, and I. Smurov: *J. Mater. Process. Technol.*, 2010, vol. 210, pp. 1624–31.
32. O. Grong: *Metallurgical Modelling of Welding Materials Modelling Series*, The Institute of Materials, London, 1994.
33. S.S. Babu, in *Proceedings of 10th International Conference on Trends in Welding Research and 9th International Welding Symposium of Japan Welding Society (9WS)*, AWS, 2017.
34. A. Plotkowski, M.M. Kirka, and S.S. Babu: *Addit. Manuf.*, 2017, vol. 18, pp. 256–68.
35. M. St. Weglowski, S. Blacha, and A. Philips: *Vacuum*, 2016, vol. 130, pp. 72–92.
36. M. Gaumann, C. Bezencon, P. Canalis, and W. Kurz: *Acta Mater.*, 2001, vol. 49, pp. 1051–62.
37. Y. Fujita, K. Saida, and K. Nishimoto: *Mater. Sci. Forum*, 2008, vols. 580–582, pp. 67–70.
38. J.-W. Park, J.M. Vitek, S.S. Babu, and S.A. David: *Sci. Technol. Weld. Join.*, 2004, vol. 9, pp. 472–82.
39. M.L. Griffith, D.M. Keicher, C.L. Atwood, J.A. Romero, J.E. Smugeresky, L.D. Harwell, and D.L. Greene, 7th Solid Freeform Fabrication (SFF) Proceedings, 1996, pp. 125–31.
40. D.D. Gu, W. Meiners, K. Wissenbaj, and R. Poprawe: *Int. Mater. Rev.*, 2012, vol. 57, pp. 136–64.
41. Simulation of Additive Manufacturing Process (SAMP), Applied Optimization, <http://appliedocom.mydomain.com/Applied/samp/>. Accessed March 2018.
42. S.S. Babu, in *Proceedings of the International conference on Solid-Solid Phase Transformations in Inorganic Materials 2015*, Jun 28 to July 3, 2015, M. Millitzer, G. Botton, L.-Q. Chen, J. How, C. Sinclair, and H. Zurob, TMS, pp. 1019-26.
43. R.R. Dehoff, W.J. Sames, M.K. Kirka, H. Bilheux, A.S. Tremsin, and S.S. Babu: *Mater. Sci. Technol.*, 2015, vol. 31, pp. 931–38.
44. R. Trivedi and W. Kurz: *Int. Mater. Rev.*, 1994, vol. 39, pp. 49–74.
45. J. Dantzig and M. Rappaz: *Solidification*, 2nd ed., EPFL Press, Lausanne, 2017.
46. S.S. Babu, J.W. Elmer, S.A. David, and J.M. Vitek: *Acta Mater.*, 2002, vol. 50, pp. 4763–81.
47. S.S. Babu: *Int. Mater. Rev.*, 2009, vol. 54, pp. 333–67.
48. S. Fukumoto and W. Kurz: *ISIJ Int.*, 1999, vol. 39, pp. 1270–79.
49. N. Raghavan, A. Plotkowski, R.R. Dehoff, J.A. Turner, M.K. Kirka, and S.S. Babu: *Acta Mater.*, 2017, vol. 140, pp. 375–87.
50. N. Raghavan, S.S. Babu, R.R. Dehoff, S. Pannala, S. Simunovic, M.K. Kirka, J. Turner, and N. Carlson: *Acta Mater.*, 2016, vol. 112, pp. 303–14.
51. M. Haines, C. Frederick, A. Plotkowski, and S.S. Babu, Unpublished research, UTK, 2018.
52. Y.S. Lee, M.M. Kirka, N. Raghavan, and, R.R. Dehoff, in *Proceedings of Solid Freeform Fabrication 2017*, pp. 1006-17.
53. <https://youtu.be/9sFSSFCTkCs>.
54. X. He, P.W. Fuerschbach, and T. DebRoy: *J. Phys. D Appl. Phys.*, 2003, vol. 12, pp. 1388–98.
55. J. Raplee, A. Plotkowski, M. Kirka, R. Dinwiddie, A. Okello, R.R. Dehoff, and S.S. Babu: *Sci. Rep.*, 2017, vol. 7, p. 43554.
56. S.S. Babu, M.K. Miller, J.M. Vitek, and S.A. David: *Acta Mater.*, 2001, vol. 49, pp. 4149–60.
57. Y.S. Lee, M.M. Kirka, S. Kim, N. Sridharan, A. Okello, R.R. Dehoff, and S.S. Babu: submitted to *Metall. Mater. Trans. A*, 2018.
58. Z. Feng, S.A. David, T. Zacharia, and C.L. Tsai: *Sci. Technol. Weld. Join.*, 1997, vol. 2, pp. 11–19.
59. Y. Yang, S.S. Babu, S. Vaze, J. Kikel and D. Dewees: *Proceedings of Trends in Welding Research*, ASM International, Pine Mountain, 2008.
60. X. Wang, G. Han, C. Cui, S. Guan, T. Jin, X. Sun, and Z. Hu: *Metall. Mater. Trans. A*, 2016, vol. 47A, pp. 5994–6003.
61. P. Fernandez-Zelaia, B.S. Adair, V.M. Barker, and S.D. Antolovich: *Metall. Mater. Trans.*, 2015, vol. 46A, pp. 5596–5609.
62. S.D. Antolovich and R.W. Armstrong: *Prog. Mater. Sci.*, 2014, vol. 59, pp. 1–160.
63. W. Dieter and G. Mook, NDI for manufacturing Anomalies in Aero-Engine Rotor Disks, in *Proceedings of ECNDT*, 2006, Berlin.
64. E. Todorov, R. Spencer, S. Gleeson, M. Jamshidinia, and S.M. Kelly, America Makes: National Additive Manufacturing Innovation Institute: Project 1: Nondestructive Evaluation (NDE) of Complex Metallic Additive Manufactured (AM) structures, AFRL-RX-WP-TR-2014-0162, Interim Report, June 2014.
65. T. Watkins, H. Bilheux, K. An, A. Payzant, R. Dehoff, C. Duty, W. Peter, C. Blue, and C. Brice: *Adv. Mater. Process.*, 2013, vol. 171, pp. 23–27.
66. S. Yoder, S. Morgan, E. Barnes, C. Kinzy, P. Nandwana, M. Kirka, S.S. Babu, V. Paquit, and R.R. Dehoff: *Addit. Manuf.*, 2018, vol. 19, pp. 184–96.
67. Y. Lee, M.M. Kirka, R.R. Dehoff, and S.S. Babu: Unpublished Research, UTK, 2018.
68. P. Prabhakar, W.J. Sames, R. Smith, R. Dehoff, and S.S. Babu: *Addit. Manuf.*, 2015, vol. 7, pp. 83–91.
69. C.A. Steed, W. Hasley, R. Dehoff, S.L. Yoder, V. Paquit, and S. Powers: *Comput. Gr.*, 2017, vol. 63, pp. 50–64.
70. C.J. Smith, S. Tamma-Williams, E. Hernandez-Nava, and I. Todd: *Sci. Rep.*, 2017, vol. 7, p. 10514.
71. P. Nandwana, A.M. Elliott, D. Sidel, A. Merriman, W.H. Peter, and S.S. Babu: *Curr. Opin. Mater. Sci.*, 2017, vol. 21, pp. 207–18.
72. R. Engeli, T. Etter, S. Hoverl, and K. Wegener: *J. Mater. Process. Technol.*, 2016, vol. 229, pp. 484–91.
73. U. Ackelid, Powder pre-processing for additive manufacturing, *US Patent # 9,661,542B2*, February 2017.
74. L.N. Carter, X. Wang, N. Read, R. Khan, M. Aristizabal, K. Essa, and M.M. Attallah: *Mater. Sci. Technol.*, 2016, vol. 32, pp. 657–61.
75. L.N. Carter, K. Essa, and M.M. Attallah: *Rapid Prototyp. J.*, 2015, vol. 21, pp. 423–32.
76. L.N. Carter, M.M. Attallah, and R.C. Reed, in *Superalloys 2012*, Proceedings edited by E.S. Huron, R.C. Reed, M.C. Hardy, M.J. Mills, R.E. Montero, P.D. Portella and J. Telesman, pp. 577-86.
77. S. Catchpole-Smith, N. Aboulkhair, L. Parry, C. Tuck, I.A. Ashcroft, and A. Clare: *Addit. Manuf.*, 2017, vol. 15, pp. 113–22.
78. Q. Ja and D. Gu: *J. Alloys Compd.*, 2014, vol. 585, pp. 713–21.
79. P.C. Collins, D.A. Brice, P. Samimi, I. Ghamarian, and H.L. Fraser: *Ann. Rev. Mater. Res.*, 2016, vol. 46, pp. 63–91.

80. R. Acharya, R. Bansal, J.J. Gambone, and S. Das: *Metall. Mater. Trans. B*, 2014, vol. 45B, pp. 2247–61.
81. N.J. Harrison, I. Todd, and K. Mumtaz: *Acta Mater.*, 2015, vol. 94, pp. 59–68.
82. T. Mukherjee, J.S. Zuback, A. De, and T. DebRoy: *Sci. Rep.*, 2016, vol. 6, p. 19717.
83. X. Wang, L.N. Carter, B. Pang, M.M. Attallah, and M.H. Loretto: *Acta Mater.*, 2017, vol. 128, pp. 87–95.
84. E. Chauvet, P. Kontis, E.A. Jagle, B. Gault, D. Raabe, C. Tassin, J.-J. Blandin, R. Dendievel, B. Vayre, S. Abed, and G. Martin: *Acta Mater.*, 2018, vol. 142, pp. 82–94.
85. E.A. Jagle, Z. Sheng, L. Wu, L. Lu, J. Risse, A. Weisheit, and D. Raabe: *JOM*, 2016, vol. 68, pp. 943–949.
86. G.H. Cao, T.Y. Sun, C.H. Wang, X. Li, M. Liu, Z.X. Zhang, P.F. Hu, A.M. Russell, R. Scheneider, D. Gerthsen, Z.J. Zhou, C.P. Li, and G.F. Chen: *Mater. Charact.*, 2018, vol. 136, pp. 398–406.
87. H.E. Helmer, C. Korner, and R.F. Singer: *J. Mater. Res.*, 2014, vol. 29, pp. 1987–96.
88. M. Ramsperger, R.F. Singer, and C. Korner: *Metall. Mater. Trans. A*, 2016, vol. 47A, pp. 1469–80.
89. C. Li, R. White, X.Y. Fang, M. Weaver, and Y.B. Guo: *Mater. Sci. Eng. A*, 2017, vol. 705, pp. 20–31.
90. K. Essa, R. Khan, H. Hassanin, M.M. Attallah, and R. Reed: *Int. J. Adv. Manuf. Technol.*, 2016, vol. 83, pp. 1835–45.
91. M. Bambach, I. Sizova, F. Silze, and M. Schnik: *J. Alloys Compd.*, 2018, vol. 740, pp. 278–87.
92. M. Ramsperger, L.M. Roncery, I. Lopez-Galilea, R.F. Singer, W. Theisen, and C. Korner: *Adv. Eng. Mater.*, 2005, vol. 17, pp. 1486–93.
93. T.G. Vilaro, C. Colin, J.D. Barout, L. Naze, and M. Sennour: *Mater. Sci. Eng. A*, 2012, vol. 534, pp. 446–51.
94. Q. Jia and D. Gu: *Opt. Laser Technol.*, 2014, vol. 62, pp. 161–71.
95. P. Kanagarajah, F. Brenne, T. Niendorf, and H.J. Maier: *Mater. Sci. Eng. A*, 2013, vol. 588, pp. 188–95.
96. K. Kunze, T. Etter, J. Grasslin, and V. Shklover: *Mater. Sci. Eng. A*, 2015, vol. 620, pp. 213–22.
97. A. Krieteberg, V. Brailovski, and S. Turenne: *Mater. Sci. Eng. A*, 2017, vol. 689, pp. 1–10.
98. G. Bi, C.-N. Sun, H.-C. Chen, F.L. Nag, and C.C.K. Ma: *Mat. Des.*, 2014, vol. 60, pp. 401–08.
99. E.R. Denlinger, J.C. Heigel, P. Michaleris, and T.A. Palmer: *J. Mater. Process. Technol.*, 2015, vol. 215, pp. 123–31.
100. Z. Wang, E. Denlinger, P. Michaleris, A.D. Stoica, D. Ma, and A.M. Beese: *Mater. Des.*, 2017, vol. 113, pp. 169–177.
101. M.M. Attallah, R. Jennings, X.Q. Wang, and L.N. Carter: *MRS Bull.*, 2016, vol. 41, pp. 758–64.
102. S.K. Everton, M. Hirsch, P. Stravroulakis, R.K. Leach, and A.T. Clare: *Mater. Des.*, 2016, vol. 95, pp. 431–45.
103. M. Hirsch, R. Patel, W. Li, G. Guan, R.K. Leach, S.D. Sharples, and A.T. Clare: *Addit. Manuf.*, 2017, vol. 13, pp. 135–42.
104. Z. Townsend, N. Senin, L. Blunt, R.K. Leach, and J.S. Taylor: *Precis. Eng.*, 2016, vol. 46, pp. 34–47.
105. M. Islam, T. Purtonen, H. Piili, A. Salminen, and O. Nyrhila: *Phys. Proc.*, 2013, vol. 41, pp. 835–42.
106. L. Song, W. Huang, X. Han, and J. Mazumder: *IEEE Trans Ind. Electron.*, 2017, vol. 64, pp. 633–42.
107. National academics of Sciences, Engineering, and Medicine 2016, in Predictive Theoretical and Computational Approaches for Additive Manufacturing: Proceedings of a Workshop. The National Academics Press, Washington, DC. <https://doi.org/10.17226/23646>.
108. M. Thomas, G.J. Baxter, and I. Todd: *Acta Mater.*, 2016, vol. 108, pp. 26–35.
109. P. Nie, O.A. Ojo, and Z. Li: *Acta Mater.*, 2014, vol. 77, pp. 85–95.
110. T.M. Rodgers, J.D. Madison, and V. Tikare: *Comput. Mater. Sci.*, 2017, vol. 135, pp. 78–89.
111. R. Acharya, J.A. Sharon, and A. Staroselsky: *Acta Mater.*, 2017, vol. 124, pp. 360–71.
112. H.L. Wei, J. Mazumder, and T. DebRoy: *Sci. Rep.*, 2015, vol. 5, p. 16446.
113. T. Mukherjee, W. Zhang, and T. DebRoy: *Comput. Mater. Sci.*, 2017, vol. 126, pp. 360–72.